ORNL/SPR-2023/2926

Phase Field Sintering Simulations of Tagged UO_2

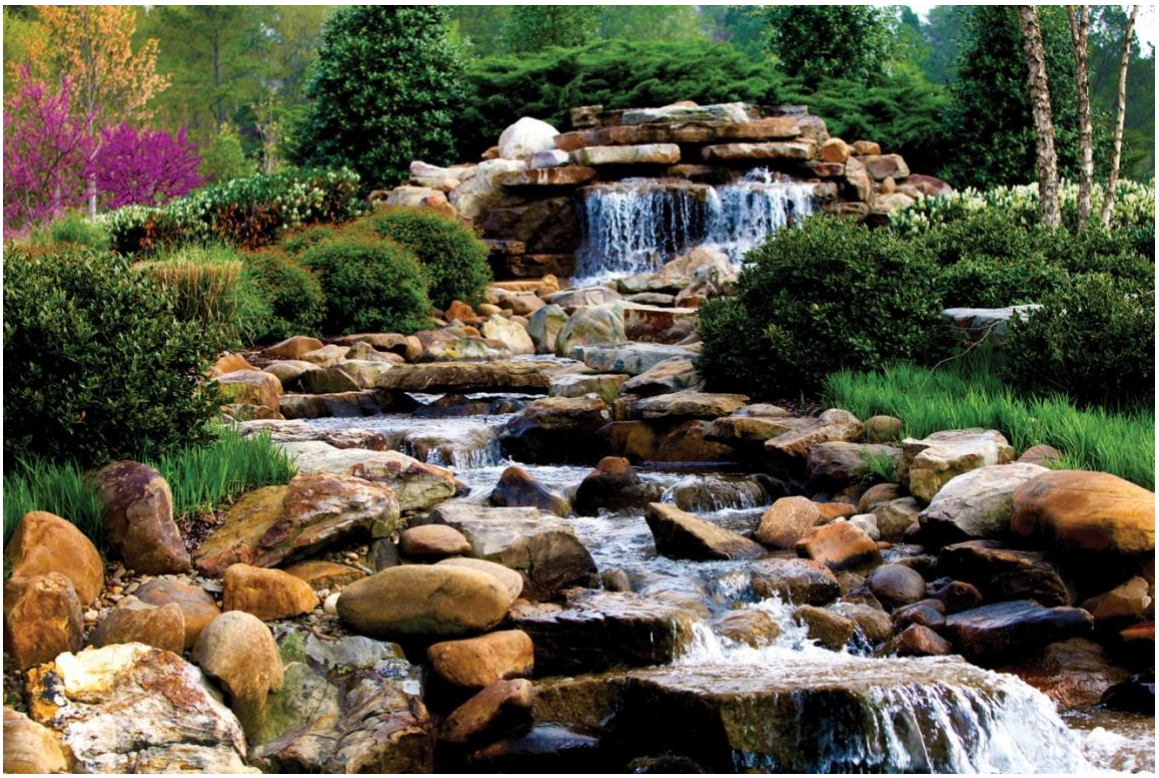

Ian Greenquist
Amani Cheniour
Tashiema Ulrich
Andrew Kercher
Ashley Shields

August 2023

OAK RIDGE National Laboratory

ORNL IS MANAGED BY UT-BATTELLE LLC FOR THE US DEPARTMENT OF ENERGY

ORNL/SPR-2023/2926

Nonproliferation Research and Development

PHASE FIELD SINTERING SIMULATIONS OF TAGGED UO_2

Ian Greenquist
Amani Cheniour
Tashiema Ulrich
Andrew Kercher
Ashley Shields

August 2023

Prepared by
OAK RIDGE NATIONAL LABORATORY
Oak Ridge, TN 37831
managed by
UT-BATTELLE LLC
for the
US DEPARTMENT OF ENERGY
under contract DE-AC05-00OR22725

CONTENTS

LIST OF FIGURES

ABSTRACT

Isotopic taggants are being considered as an additive for UO_2 manufacturing to improve nuclear security. Before taggants can be adopted, it must be determined whether taggants have any effect on the fuel microstructure or performance. As part of this effort, a grand potential formulation of the phase field method was used to model untagged, Cr-tagged, and Fe-tagged UO_2. The simulations were compared to determine whether the taggants had any effect on fuel density or grain size. The results suggest that the taggants will not affect the density or grain size, but these findings may not be reliable because of high uncertainty. Causes of the uncertainty were discussed, and future work is proposed to reduce the model uncertainty.

1. INTRODUCTION

The nuclear security community is investigating the addition of isotopic taggants in nuclear fuels to aide in and expedite the provenance assessment of nuclear materials that are found outside of regulatory control [1, 2]. These taggants would consist of small concentrations of one or more isotopes added to the fuel during manufacturing, similar to dopants. The taggants would be added during fuel manufacturing to make the fuels easily identifiable to the facility they were manufactured in. As part of this effort, the effect of taggants on fuel performance must be quantified. Dopants such as Cr can change the fuel microstructure and affect the fission gas release (FGR) behavior of fuel during reactor operation [3–10]. Therefore, it is important to understand the effects of each candidate taggant on the fuel microstructure and how that microstructure affects the fuel performance.

UO_2 fuel pellets are manufactured via a process called sintering in which the solid material is heated to nearly melting, and the individual particles coalesce into a single porous polycrystalline mass. Sintering is governed by diffusion and grain growth effects. The thermodynamics and kinetics of the process are complex and governed by the interactions between point defects, grain boundaries (GBs), surfaces, pressure, and temperature. Furthermore, sintering is highly sensitive to relatively small changes in factors such as the O/U ratio of the fuel, the sintering atmosphere, and the presence of minor impurities (e.g., dopants or taggants) [11]. The porosity and grain size distribution that sintering creates affects the performance of UO_2 during reactor operation, and the largest effect is on FGR. Large-grain UO_2 undergoes less FGR than small-grain UO_2. Furthermore, adding a dopant such as Cr will increase the grain size of the fuel [4]. However, the mechanism by which dopants affect the grain growth is not fully understood. A recent model proposed by Cooper et al. suggests that the dopants change the charge state of the fuel atoms. The conservation-of-charge principle requires that additional vacancies form in the material to offset the charge [8, 9]. This mechanism led to the development of a density functional theory (DFT) model to calculate the U-vacancy concentration and efforts to model Cr- and Mn-doped UO_2 sintering using the phase field method [9, 10]. A similar approach can now be used to evaluate the microstructural effects of taggants on UO_2.

The phase field method uses field variables to describe conserved and non-conserved variables [12]. The method can predict microstructure evolution without the need for interface tracking, thereby reducing the computational complexity compared to other microstructural models. At least three phase field models have been developed for sintering: the Wang rigid body motion model in 2006 [13], the 2019 grand potential formulation by Hötzer et al. [14], and another grand potential formulation developed by Aagesen et al. [15] in 2018 and applied to sintering by Greenquist et al. in 2020 [16]. This work uses the Aagesen–Greenquist formulation [10] and applies Cooper et al.–calculated vacancy concentrations to model tagged sintering [9].

None of the phase field sintering models listed above fully capture sintering kinetics. For example, none of the models can model sintering atmosphere composition and pressure or variations in the O/U ratio of the fuel. In addition, limitations on the simulation size and high uncertainty in the self-diffusion coefficient of U have contributed to high uncertainty in the sintering model to the point that full model validation is not feasible [16]. The model can only be used to make relative comparisons between dopant behaviors [10]. For these reasons, the predictions made by these models require experimental validation before being used to make design decisions.

Section 2 provides a description of the phase field model used. Although some values are derived, this description is only a summary. More complete derivations are described in the literature [15, 16]. Section 3 describes the simulations performed for this work, including descriptions of how the initial condition is generated and how the density is calculated. Section 4 describes the simulation results. Finally, Section 5 provides a summary of the work performed, draws conclusions based on the results, and recommends future work to improve the model's accuracy.

2. MODEL DESCRIPTION

Non-conserved field variables include *N* order parameters (OPs), $\vec{\eta} = \{\eta_1, \eta_2, \dots, \eta_N\}$, which represent the individual crystal grains that make up the matrix (*m*) phase and one OP, ϕ, that describes the void (*v*) phase. The OPs are governed by the Allen Cahn equation [17]:

$$\begin{aligned} \frac{\partial \phi}{\partial t} &= -L_v \frac{\delta \Omega}{\delta \phi}, \\ \frac{\partial \eta_i}{\partial t} &= -L_m \frac{\delta \Omega}{\delta \eta_i}, \end{aligned} \tag{1}$$

where L_v and L_m are the phase mobilities for the void and matrix phases, respectively, and Ω is the grand potential function. The grand potential function is [15] given by Eq. (2):

$$\Omega = \int_V [\epsilon f_B + \kappa f_G + h_m \omega_m + (1 - h_m)\omega_v] dV , \tag{2}$$

where V is the volume, ϵ is the bulk energy coefficient, κ is the gradient energy coefficient, f_B is the bulk energy function, f_G is the gradient energy function, h_m is a switching function, and ω_m and ω_v are the local potential density functions for the *m* and *v* phases, respectively. The bulk free energy has the form

$$f_B = \left(\frac{\phi^4}{4} - \frac{\phi^2}{2}\right) + \sum_{i=1}^{N}\left(\frac{\eta_i^4}{4} - \frac{\eta_i^2}{2}\right) + \frac{3}{2}\left(\phi^2 \sum_{i=1}^{N} \eta_i^2 + \sum_{i=1}^{N-1}\sum_{j=i+1}^{N} \eta_i^2 \eta_i^2\right) + \frac{1}{4}. \tag{3}$$

This function ensures that it is energetically preferred to have exactly one OP equal to 1 and all other OPs equal to 0. The gradient energy has the form

$$f_G = \frac{1}{2}\left((\nabla\phi)^2 + \sum_{i=1}^{N} (\nabla\eta_i)^2\right). \tag{4}$$

This form applies an energy penalty to high gradients, thus ensuring the interfaces between OPs are smooth.

The diffusivity of U atoms is much lower than the diffusivity of O atoms, making U the rate-limiting species [16]. Furthermore, it has been shown that the effects of interstitials are negligible in U sintering (at least in this model) [18]. Therefore, only U vacancies are considered in the model. The U vacancy density, ρ, is described by the diffusion equation

$$\frac{\partial \rho}{\partial t} = \nabla \cdot \boldsymbol{D} \nabla \rho, \tag{5}$$

where $\boldsymbol{D}$ is the diffusion tensor. Chain rule expansion can be used to describe the time derivative of ρ by the chemical potential μ and the OPs according to

$$\frac{\partial \rho}{\partial t} = \frac{\partial \rho}{\partial \mu}\frac{\partial \mu}{\partial t} + \frac{\partial \rho}{\partial \phi}\frac{\partial \phi}{\partial t} + \sum_{i=1}^{N} \frac{\partial \rho}{\partial \eta_i}\frac{\partial \eta_i}{\partial t}. \tag{6}$$

Equations (5) and (6) can then be combined into a governing equation for the chemical potential

$$\chi \frac{\partial \mu}{\partial t} = \nabla \cdot \chi \boldsymbol{D} \nabla \mu - \left(\frac{\partial \rho}{\partial \phi}\frac{\partial \phi}{\partial t} + \sum_{i=1}^{N} \frac{\partial \rho}{\partial \eta_i}\frac{\partial \eta_i}{\partial t} \right), \tag{7}$$

where $\chi = \frac{\partial \rho}{\partial \mu}$ is the susceptibility. Equations (1) and (7) are the primary governing equations of the system.

The chemical potential is a function of the phase-specific vacancy density

$$\mu = \frac{\partial f_m}{\partial \rho_m} = \frac{\partial f_v}{\partial \rho_v}, \tag{8}$$

where ρ_m and ρ_v are the phase-specific densities, and f_m and f_v are the free energies of vacancies in the *m* and *v* phases. The free energies are approximated as parabolic curves

$$\begin{aligned} f_m &= \frac{1}{2}\, k_m \left(\rho_m - \rho_m^{eq}\right)^2, \\ f_v &= \frac{1}{2} k_v \left(\rho_v - \rho_v^{eq}\right)^2, \end{aligned} \tag{9}$$

where k_m and k_v are parabolic coefficients, and ρ_m^{eq} and ρ_v^{eq} are equilibrium vacancy concentrations. The vacancy density can be defined in terms of chemical potential by combining Eqs. (8) and (9):

$$\begin{aligned} \rho_m &= \rho_m^{eq} + \frac{\mu}{k_m}, \\ \rho_v &= \rho_v^{eq} + \frac{\mu}{k_v}, \\ \rho &= h_m \rho_m + (1 - h_m)\rho_v. \end{aligned} \tag{10}$$

The susceptibility from Eq. (7) now becomes

$$\chi = \frac{h_m}{k_m} + \frac{1 - h_m}{k_v}, \tag{11}$$

and the local potential densities from Eq. (2) become

$$\begin{aligned} \omega_m &= f_m - \rho_m \mu = -\frac{1}{2} k_m \left(\rho_m^2 - \rho_m^{eq\,2}\right), \\ \omega_v &= f_v - \rho_v \mu = -\frac{1}{2} k_v \left(\rho_v^2 - \rho_v^{eq\,2}\right). \end{aligned} \tag{12}$$

The Allen Cahn mobilities from Eq. (1) can be defined according to [16]

$$\begin{aligned} L_m &= \frac{4}{3} M_{GB} \ell, \\ L_v &= 40 L_s, \end{aligned} \tag{13}$$

where M_{GB} is the GB mobility and ℓ is the interface width. The GB mobility is calculated with the Arrhenius equation

$$M_{GB} = M_0 \exp\left(-\frac{Q}{k_B T}\right), \tag{14}$$

where M_0 is the mobility prefactor, Q is the GB mobility activation energy, k_B is Boltzmann's constant, and T is the absolute temperature.

The energy coefficients ϵ and κ are described by the following equations:

$$\begin{aligned} \epsilon &= h_S \epsilon_S + (1 - h_S)\epsilon_{GB}, \\ \kappa &= h_S \kappa_S + (1 - h_S)\kappa_{GB}, \\ \epsilon_S &= 6\frac{\sigma_S}{\ell}, \;\; \epsilon_{GB} = 6\frac{\sigma_{GB}}{\ell}, \\ \kappa_S &= \frac{3}{4}\sigma_S \ell, \;\; \kappa_{GB} = \frac{3}{4}\sigma_{GB}\ell, \end{aligned} \tag{15}$$

where σ_S and σ_{GB} are the interface energies for external surfaces and GBs, respectively, and h_S is a switching function that distinguishes surfaces from GBs. Both switching functions, h_m and h_S, are derived from the same function:

$$H(\phi_0) = \begin{cases} 0, & \phi \le 0 \\ 6\left(\frac{\phi}{\phi_0}\right)^5 - 15\left(\frac{\phi}{\phi_0}\right)^4 + 10\left(\frac{\phi}{\phi_0}\right)^3, & 0 < \phi < \phi_0 \\ 1, & \phi \ge \phi_0 \end{cases}, \tag{16}$$

where ϕ_0 is a constant between 0 and 1. The switching functions are $h_m = 1 - H(1)$ and $h_S = H(0.3)$ [16].

The diffusion coefficient is represented as a tensor to differentiate between bulk, GB, and surface diffusion. The definition is taken from Ahmed et al. [19]:

$$\begin{aligned} \boldsymbol{D} &= D_B \boldsymbol{I} + D_{GB} \sum_{i=1}^{N} \sum_{j \neq i}^{N} \eta_i \eta_j \boldsymbol{T}_{GB}^{ij} + D_S \phi^2 (1 - \phi)^2 \boldsymbol{T}_S, \\ \boldsymbol{T}_{GB}^{ij} &= \boldsymbol{I} - \frac{\nabla\eta_i - \nabla\eta_j}{|\nabla\eta_i - \nabla\eta_j|} \otimes \frac{\nabla\eta_i - \nabla\eta_j}{|\nabla\eta_i - \nabla\eta_j|}, \\ \boldsymbol{T}_S &= \boldsymbol{I} - \frac{\nabla\phi}{|\nabla\phi|} \otimes \frac{\nabla\phi}{|\nabla\phi|}, \end{aligned} \tag{17}$$

where D_B is the bulk diffusion magnitude, D_{GB} is the GB diffusion magnitude, and D_S is the surface diffusion magnitude. The tensor $\boldsymbol{I}$ is the identity tensor, and $\boldsymbol{T}_{GB}^{ij}$ and $\boldsymbol{T}_S$ are the normalized directional tensors for the GBs and surfaces, respectively. The diffusion magnitudes follow the convention of Greenquist et al. [16]:

$$D_B = D_0 \exp\left(-\frac{E}{k_B T}\right),$$
$$D_{GB} = w_{GB} D_B,$$
$$D_S = w_S D_B, \tag{18}$$

where D_0 and E are the Arrhenius prefactor and migration energy, respectively, and w_{GB} and w_S are weight factors applied to the GB and surfaces, respectively.

The matrix equilibrium vacancy concentration from Eqs. (9), (10), and (12) is defined as follows:

$$\rho_m^{eq} = \rho_B + 4(\rho_{GB} - \rho_B)(1-\lambda)^2,$$
$$\lambda = \sum_{i=1}^{N} \eta_i^2, \tag{19}$$

where ρ_B and ρ_{GB} are the equilibrium solid-phase vacancy densities in the bulk (grain interiors) and on GBs, respectively.

In this model, the solid vacancy densities are the only property affected by the taggants. Therefore, they must be calculated depending on each taggant. Arrhenius functions were fit to the vacancy concentrations plotted by Cooper et al. [9] for each curve to give the following concentration curves:

$$\rho_{B,j} = \frac{c_{B,j}}{V_a},$$
$$\rho_{GB,j} = \rho_{B,j} \exp\left(\frac{E_{GB}}{k_B T}\right),$$
$$c_{B,j} = A_j \exp\left(\frac{B_j}{k_B T}\right), \tag{20}$$

where $\rho_{B,j}$ and $\rho_{GB,j}$ are the bulk and GB equilibrium vacancy densities for taggant j, $c_{B,j}$ is the vacancy concentration, and V_a is the atomic volume of a vacancy. The Arrhenius constants A_j and B_j are fit to individual taggants. Finally, E_{GB} is a GB defect formation energy. For untagged fuel, the Arrhenius constants have the following values:

$$A_{un} = \begin{cases} 2.751 \times 10^{-5}, & T < 1108.6 \\ 1.957 \times 10^{-18}, & T \geq 1108.6 \end{cases},$$
$$B_{un} = \begin{cases} 0.26, & T < 1108.6 \\ 3.15, & T \geq 1108.6 \end{cases}. \tag{21}$$

For Al-, Cr-, Fe-, Ti-, and V-tagged fuels, the values are as follows:

$$A_{Al} = A_{un},$$
$$B_{Al} = B_{un}, \tag{22}$$

$$A_{Cr} = \begin{cases} A_{un}, & T < 1808.3 \\ 8.357 \times 10^{-3}, & T \geq 1808.3 \end{cases},$$
$$B_{Cr} = \begin{cases} B_{un}, & T < 1808.3 \\ -2.46, & T \geq 1808.3 \end{cases}, \tag{23}$$

$$A_{Fe} = \begin{cases} A_{un}, & T < 1896.4 \\ 3.048 \times 10^{-4}, & T \geq 1896.4 \end{cases},$$
$$B_{Fe} = \begin{cases} B_{un}, & T < 1896.4 \\ -2.19, & T \geq 1896.4 \end{cases}, \tag{24}$$

$$A_{Ti} = \begin{cases} A_{un}, & T < 1786.4 \\ 6.495 \times 7, & T \geq 1786.4 \end{cases}, \tag{25}$$

$$B_{Ti} = \begin{cases} B_{un}, & T < 1786.4 \\ -0.93, & T \geq 1786.4 \end{cases},$$
$$A_V = \begin{cases} A_{un}, & T < 1896.4 \\ 8.959 \times 10^4, & T \geq 1896.4 \end{cases},$$
$$B_V = \begin{cases} B_{un}, & T < 1718.4 \\ -4.58, & T \geq 1718.4 \end{cases}. \quad (26)$$

The untagged and tagged bulk U-vacancy concentrations produced by Eqs. (20)–(26) are shown in Figure 1. Because all taggants increase the U-vacancy concentration, the taggants are expected to increase the sintering rate, thus increasing the density and average grain size.

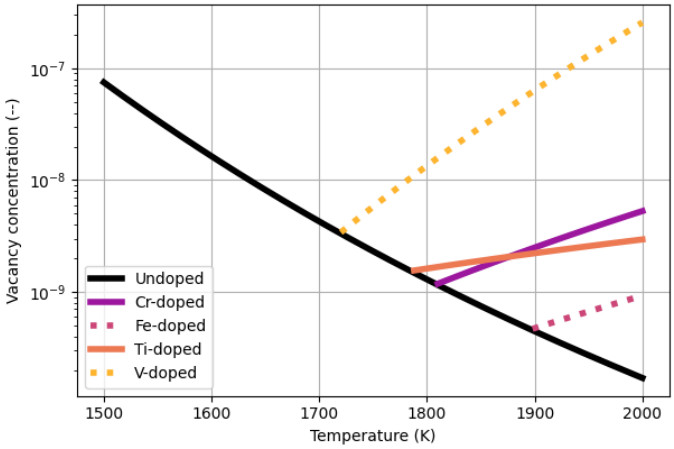

Figure 1. Equilibrium bulk U-vacancy concentrations as a function of temperature for untagged, Cr-, Fe-, Ti-, and V-tagged UO_2. These values do not match the values used in the previous doped sintering study [10]. The 2020 paper used an updated potential for the vibrational entropy in the DFT formulation, but only Cr and Mn were considered in that study. Therefore, the concentrations from the 2018 paper were used for this work [9]. The 2020 concentrations are approximately 100 times higher than the 2018 concentrations.

The remaining constant values used in the model are provided in Table 1 along with units and references. The number of OPs, N; the interface thickness, ℓ; and the temperature, T, are set in Section 3 because they are simulation-specific parameters.

Table 1. Constant values used in the grand potential sintering model

Name	Value	Units	Ref.
ρ_v^{eq}	$1/V_a$	nm^{-3}	—
σ_F	19.7	$eV\ nm^{-2}$	[20]
σ_{GB}	9.86	$eV\ nm^{-2}$	[21]
D_0	8.33×10^9	$nm^2\ s^{-1}$	[16]
E	3.608	eV	[16]
E_{GB}	1.5	eV	[10]
k_s	26.8	$eV\ nm^{-3}$	[18]
k_v	26.8	$eV\ nm^{-3}$	[18]
M_0	1.4759×10^9	$nm^4\ eV^{-1}\ s^{-1}$	[22]
Q	2.77	eV	[22]
V_a	0.04092	nm^3	[23]
w_S	10^9	—	[16]
w_{GB}	10^6	—	[16]

3. SIMULATION SETUP

The simulation was performed using the phase field code MARMOT [24], developed and maintained by Idaho National Laboratory (INL). All the necessary tools and models for grand potential sintering simulations are included in MARMOT. The simulations were performed on INL's Sawtooth cluster computer [25].

The first step to designing the simulation is to determine the number of particles and the particle size distribution. A uniform particle size was selected because it facilitates a relatively high interface width, which in turn allows for a coarser mesh and lower computational cost. This decision should not significantly affect the sintering results because the initial particle size distribution only negligibly affects the sintering behavior [11]. The particles were sized at 700 nm in diameter to match the average diameter of particles sintered in the experimental portion of this project. The particle sizes were estimated by measuring distances on images taken of the unsintered powder, such as the one shown in Figure 2.

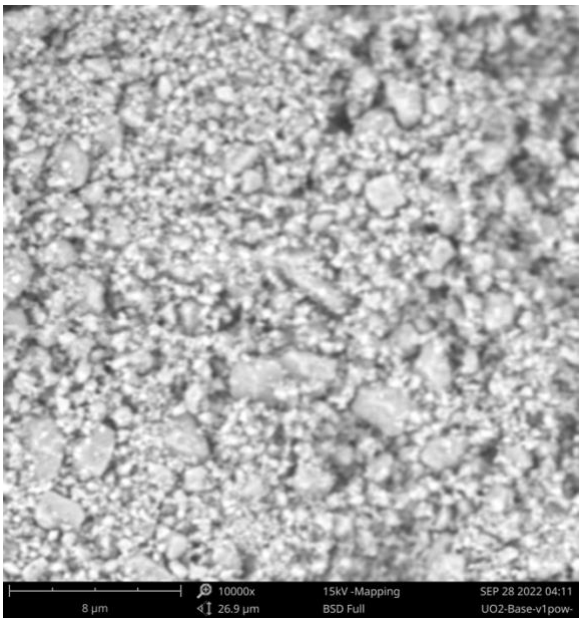

Figure 2. Example image of unsintered UO_2 powder used to estimate the average particle size.

To limit the mesh size, a cubic mesh with cubic elements was used. The mesh was 10,000 nm per side, and elements were 100 nm per side. This element size/particle size ratio required that the interface width, ℓ, be set to 300 nm. To maintain an external face to act as a vacancy sink and prevent contact with the mesh sides, particles were limited to a 7,200 nm region in the center of the domain. Trial and error determined that approximately 600 particles fit within this region, so 600 particles were used. A custom Python script based on elastic collision dynamics was used to randomly arrange the particles in a single compact. The compact is shown in Figure 3. The Python script also used the Greedy coloring algorithm to assign the particles among 26 OPs such that no two adjacent particles were assigned to the same OP. MARMOT's built-in GrainTracker algorithm was used to reassign OPs and prevent grains from coalescing during the simulations [26].

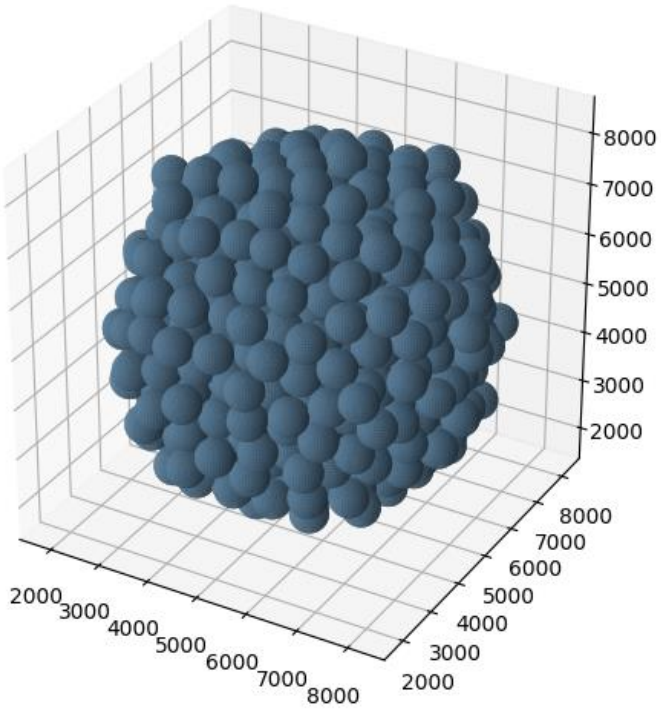

Figure 3. The initial powder compact containing 600 particles was generated by a Python script.

Three cases were simulated: untagged, Cr-tagged, and Fe-tagged. These cases were chosen to match experimentally tested materials. The sintering temperature was set to match the experimental conditions of 1,700°C. The particles began at room temperature (27°C) and were heated at a rate of 7°C min^{-1} and reached their peak temperature at 4 h. They stayed at that temperature until the particles coalesced into a single crystal grain.

The sintered density was measured using the Monte Carlo (MC) technique applied in previous studies [16]. A convex hull was constructed around the particle/grain centers, the particles were assumed to be perfect spheres, and MC integration calculated the relative density using a set of random MC points. An example of this technique is shown in Figure 4. Because of the stochastic nature of this technique, some noise is expected in the density measurements.

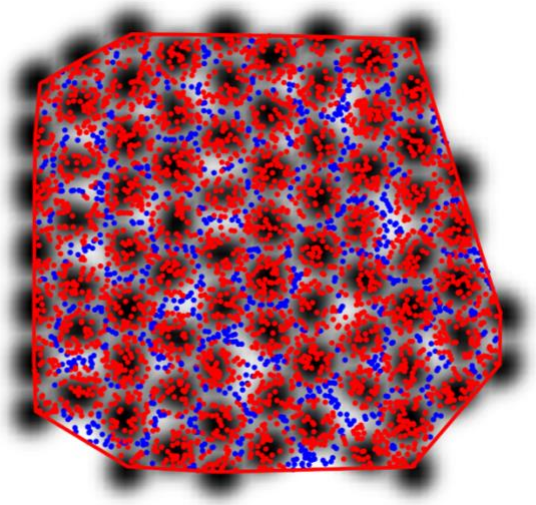

Figure 4. 2D example of the density measurement technique. The convex hull (red) and MC points (red and blue) are superimposed over an image of the phase field ($\lambda = 0$ is white, and $\lambda = 1$ is black). Points that are within the particles are red and points that are over a void are blue. The relative density is the ratio of the number of red points to total points.

4. RESULTS

The Cr-tagged simulation ran to completion, reaching a single grain after 5.13 h. The untagged and Fe-tagged simulations crashed at 4.54 and 4.19 h, respectively. The cause of the crashes is unclear. However, because all three simulations reached the peak sintering temperature, it was determined the results could be analyzed. The progression of the Cr-tagged simulation is shown in Figure 5. The density (calculated using 8,000 MC points per time step) and average grain size of all three cases are shown in Figure 6.

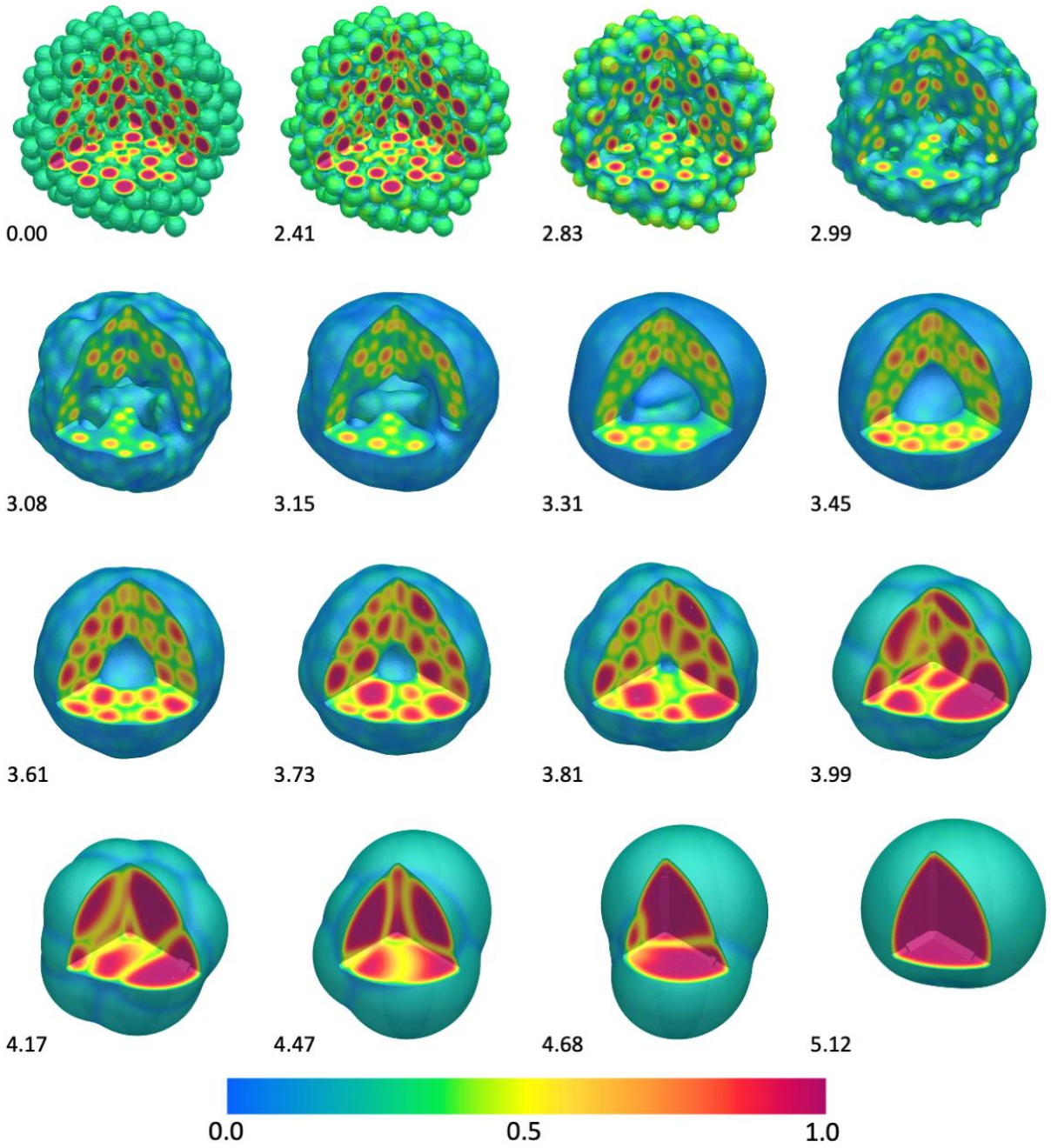

Figure 5. Simulation progress of the Cr-tagged case. Only the portions of the mesh where $\phi \leq 0.5$ are shown. One-eighth of the mesh has been cut out to facilitate visualization of the interior structure. The color represents λ. The time in hours is shown next to each image.

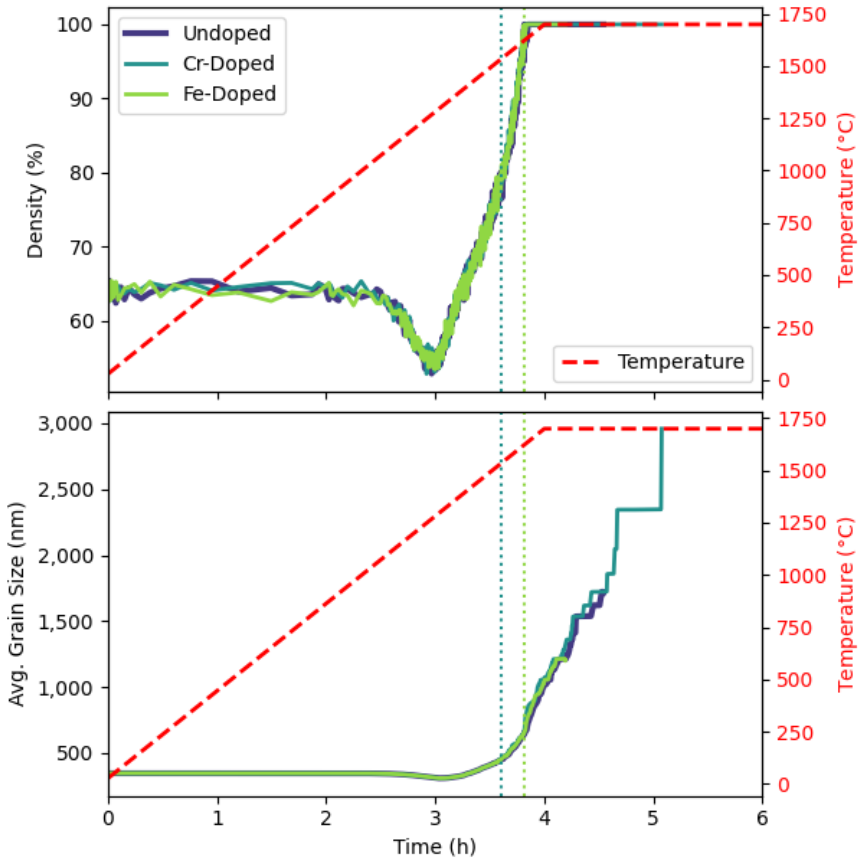

Figure 6. Density (top) and average grain size (bottom) of three sintering simulations. The simulation temperature is shown in red for reference along with the times at which both taggants vacancy densities diverged from the untagged vacancy density according to Eqs. (21)–(26).

The density increased so fast that the simulations all reached 100% density before reaching the peak temperature. This behavior is consistent with previous results [10, 16]. As mentioned in Section 1, two significant sources of uncertainty exist in the model that may affect this behavior. First, the self-diffusion coefficient of U in UO_2 is subject to an abnormally high uncertainty [16]. Even relatively small variations in this value can significantly change the sintering rate. Second, sintering is a size-dependent process. The relatively small number of particles that can be simulated results in faster sintering rates than would occur in experiment-sized simulations.

For both the Cr- and Fe-tagged cases, the densification rate was compared against the undoped case in the time frame between the vacancy concentrations diverging and one simulation crashing. During this time, the Cr-tagged grains grew at a rate of 22.7 nm min^{-1} compared with 22.5 nm min^{-1} for the untagged case over the same time. The Fe-tagged grains grew at a rate of 24.2 nm min^{-1} compared with 25.7 nm min^{-1} for the untagged case over the same time. This behavior contradicts the previous application of the Aagesen–Greenquist formulation to tagged sintering [10], which showed Cr-taggants accelerating densification by 0.74% and grain growth by 230%. It also contradicts experimental measurements which show the density increasing by 1–2% and grain growth accelerating by up to 700% [27]. This discrepancy is likely due to the vacancy density curves used in this work, as discussed Section 2.

5. CONCLUSIONS

A series of phase field simulations using a grand potential formulation was designed to predict the effects of two taggants on the microstructure of sintered UO_2. The formulation was described and established; the simulation parameters were described. The methods of generating the initial conditions and measuring the density were described. The simulation was set up with 600 initial particles—significantly more than the 113 and 100 particles used in previous works [10,16]. This increase was accomplished by optimizing the initial condition to limit the mesh size, optimizing the GrainTracker algorithm to reduce the number of variables [26], optimizing the PETSc solver options used by MARMOT to solve the governing equations [28,29], and by pre-splitting the mesh to run on the cluster more efficiently [30]. Simulations were performed with two taggants and untagged fuel. The results show that the taggants have no effect on the densification and grain growth rates. This result is promising for the present taggant study. However, the result is questionable for several reasons. First, it contradicts experimental studies and previous simulations using the same methodology [10]. Second, the model is subject to several sources of significant uncertainty that have already been discussed. Third, uncertainty in the equilibrium vacancy concentrations has carried over to these predictions. Therefore, the most reasonable conclusion that can be drawn is that the uncertainty of the grand potential sintering model is too high to yield meaningful predictions.

However, the presence of any of the taggants listed in Eqs. (21)–(26) is unlikely to result in smaller grains or reduced density. The Cooper et al. DFT model predicts that all the taggants would either have no effect or would increase the sintering rate. Furthermore, the work of Cooper et al. assumed an ideal dopant concentration in order to maximize the effects of the dopants [9], but this work suggests that a smaller dopant effect—one that could potentially be achieved by a smaller concentration—would have a reduced effect or possibly no effect. Unfortunately, nothing in this work can determine what such a concentration would be or whether it would be a sufficiently detectable amount for use as a taggant.

Future work should include updating the DFT models of all the taggants being considered to reduce the uncertainty of those input values. This study should, if possible, also consider multiple concentrations of the taggants. Furthermore, work is needed to reduce the uncertainty of the U self-diffusion coefficient and to make the phase field simulation tools more efficient (so that more particles can be simulated) and to prevent simulations from crashing. Once those tasks are complete, these simulations can be repeated and used to make updated predictions.

ACKNOWLEDGEMENTS

This material is based upon work supported by the US National Nuclear Security Administration's Office of Defense Nuclear Nonproliferation Research and Development under contract number DE-AC05-00OR22725. This research made use of the resources of the High Performance Computing Center at Idaho National Laboratory, which is supported by the Office of Nuclear Energy of the US Department of Energy and the Nuclear Science User Facilities under Contract No. DE-AC07-05ID14517.

BIBLIOGRAPHY

[1] B.A. Wilson, A. Conant, T.L. Ulrich, A. Kercher, L.R. Sadergaski, T. Gerczak, A.T. Nelson, C.M. Petrie, J. Harp, A.E. Shields, Nuclear fuel irradiation testbed for nuclear security applications, Front. Nucl. Energy. 2 (2023) 13. https://doi.org/10.3389/fnuen.2023.1123134.

[2] I.D. Hutcheon, M.J. Kristo, K.B. Knight, P.O. Box, CHAPTER 13: NONPROLIFERATION NUCLEAR FORENSICS, Lawrence Livermore National Laboratory, Livermore, California USA, 2015.

[3] K.C. Radford, J.M. Pope, UO2 fuel pellet microstructure modification through impurity additions, J. Nucl. Mater. 116 (1983) 305–313. https://doi.org/10.1016/0022-3115(83)90116-2.
[4] J. Arborelius, K. Backman, L. Hallstadius, M. Limback, J. Nillson, B. Rebensdorff, G. Zhou, K. Kitano, R. Lofstrom, G. Ronnberg, Advanced Doped Uo2 Pellets in Lwr Applications, J. Nucl. Sci. Technol. 43 (2006) 967–976. https://doi.org/10.1080/18811248.2006.9711184.
[5] T. Cardinaels, K. Govers, B. Vos, S. Van den Berghe, M. Verwerft, L. de Tollenaere, G. Maier, C. Delafoy, Chromia doped UO2 fuel: Investigation of the lattice parameter, J. Nucl. Mater. 424 (2012) 252–260. https://doi.org/10.1016/j.jnucmat.2012.02.025.
[6] V. Peres, L. Favergeon, M. Andrieu, J.C. Palussière, J. Balland, C. Delafoy, M. Pijolat, High temperature chromium volatilization from Cr2O3 powder and Cr2O3-doped UO2 pellets in reducing atmospheres, J. Nucl. Mater. 423 (2012) 93–101. https://doi.org/10.1016/j.jnucmat.2012.01.001.
[7] Ch. Riglet-Martial, Ph. Martin, D. Testemale, C. Sabathier-Devals, G. Carlot, P. Matheron, X. Iltis, U. Pasquet, C. Valot, C. Delafoy, R. Largenton, Thermodynamics of chromium in UO2 fuel: A solubility model, J. Nucl. Mater. 447 (2014) 63–72. https://doi.org/10.1016/j.jnucmat.2013.12.021.
[8] M.W.D. Cooper, S.T. Murphy, D.A. Andersson, The defect chemistry of UO2±x from atomistic simulations, J. Nucl. Mater. 504 (2018) 251–260. https://doi.org/10.1016/j.jnucmat.2018.02.034.
[9] M.W.D. Cooper, C.R. Stanek, D.A. Andersson, The role of dopant charge state on defect chemistry and grain growth of doped UO2, Acta Mater. 150 (2018) 403–413. https://doi.org/10.1016/j.actamat.2018.02.020.
[10] I. Greenquist, M. Tonks, M. Cooper, D. Andersson, Y. Zhang, Grand potential sintering simulations of doped UO2 accident-tolerant fuel concepts, J. Nucl. Mater. 532 (2020) 152052. https://doi.org/10.1016/j.jnucmat.2020.152052.
[11] I. Greenquist, M.R. Tonks, Y. Zhang, Review of sintering and densification in nuclear fuels: Physical mechanisms, experimental results, and computational models, J. Nucl. Mater. 507 (2018) 381–395. https://doi.org/10.1016/j.jnucmat.2018.03.046.
[12] L.-Q. Chen, Phase-Field Models for Microstructure Evolution, Annu. Rev. Mater. Res. 32 (2002) 113–140. https://doi.org/10.1146/annurev.matsci.32.112001.132041.
[13] Y.U. Wang, Computer modeling and simulation of solid-state sintering: A phase field approach, Acta Mater. 54 (2006) 953–961. https://doi.org/10.1016/j.actamat.2005.10.032.
[14] J. Hötzer, M. Seiz, M. Kellner, W. Rheinheimer, B. Nestler, Phase-field simulation of solid state sintering, Acta Mater. 164 (2019) 184–195. https://doi.org/10.1016/j.actamat.2018.10.021.
[15] L.K. Aagesen, Y. Gao, D. Schwen, K. Ahmed, Grand-potential-based phase-field model for multiple phases, grains, and chemical components, Phys. Rev. E. 98 (2018) 023309. https://doi.org/10.1103/PhysRevE.98.023309.
[16] I. Greenquist, M.R. Tonks, L.K. Aagesen, Y. Zhang, Development of a microstructural grand potential-based sintering model, Comput. Mater. Sci. 172 (2020) 109288. https://doi.org/10.1016/j.commatsci.2019.109288.
[17] S.M. Allen, J.W. Cahn, A microscopic theory for antiphase boundary motion and its application to antiphase domain coarsening, Acta Metall. 27 (1979) 1085–1095. https://doi.org/10.1016/0001-6160(79)90196-2.
[18] I. Greenquist, M. Tonks, Y. Zhang, Analysis of the impact of fuel microstructure on irradiation-enhanced densification using grand potential simulations, Ann. Nucl. Energy. 151 (2021) 107858. https://doi.org/10.1016/j.anucene.2020.107858.
[19] K. Ahmed, C.A. Yablinsky, A. Schulte, T. Allen, A. El-Azab, Phase field modeling of the effect of porosity on grain growth kinetics in polycrystalline ceramics, Model. Simul. Mater. Sci. Eng. 21 (2013) 065005. https://doi.org/10.1088/0965-0393/21/6/065005.
[20] R.O.A. Hall, M.J. Mortimer, D.A. Mortimer, Surface energy measurements on UO2 — A critical review, J. Nucl. Mater. 148 (1987) 237–256. https://doi.org/10.1016/0022-3115(87)90017-1.

[21] P.V. Nerikar, D.C. Parfitt, L.A. Casillas Trujillo, D.A. Andersson, C. Unal, S.B. Sinnott, R.W. Grimes, B.P. Uberuaga, C.R. Stanek, Segregation of xenon to dislocations and grain boundaries in uranium dioxide, Phys. Rev. B. 84 (2011) 174105. https://doi.org/10.1103/PhysRevB.84.174105.
[22] J.B. Ainscough, B.W. Oldfield, J.O. Ware, Isothermal grain growth kinetics in sintered UO2 pellets, J. Nucl. Mater. 49 (1973) 117–128. https://doi.org/10.1016/0022-3115(73)90001-9.
[23] M. Idiri, T. Le Bihan, S. Heathman, J. Rebizant, Behavior of actinide dioxides under pressure: UO2 and ThO2, Phys. Rev. B. 70 (2004) 014113. https://doi.org/10.1103/PhysRevB.70.014113.
[24] M.R. Tonks, D. Gaston, P.C. Millett, D. Andrs, P. Talbot, An object-oriented finite element framework for multiphysics phase field simulations, Comput. Mater. Sci. 51 (2012) 20–29. https://doi.org/10.1016/j.commatsci.2011.07.028.
[25] S.J. Parker, Anderson, Nuclear Science User Facilities High Performance Computing Fiscal Year 2022 Annual Report, Idaho National Laboratory, Idaho Falls, Idaho, 2023.
[26] C.J. Permann, M.R. Tonks, B. Fromm, D.R. Gaston, Order parameter re-mapping algorithm for 3D phase field model of grain growth using FEM, Comput. Mater. Sci. 115 (2016) 18–25. https://doi.org/10.1016/j.commatsci.2015.12.042.
[27] L. Bourgeois, Ph. Dehaudt, C. Lemaignan, A. Hammou, Factors governing microstructure development of Cr2O3-doped UO2 during sintering, J. Nucl. Mater. 297 (2001) 313–326.
[28] Satish Balay, Shrirang Abhyankar, Mark F. Adams, Steven Benson, Jed Brown, Peter Brune, Kris Buschelman, Emil M. Constantinescu, Lisandro Dalcin, Alp Dener, Victor Eijkhout, Jacob Faibussowitsch, William D. Gropp, Václav Hapla, Tobin Isaac, Pierre Jolivet, Dmitry Karpeev, Dinesh Kaushik, Matthew G. Knepley, Fande Kong, Scott Kruger, Dave A. May, Lois Curfman McInnes, Richard Tran Mills, Lawrence Mitchell, Todd Munson, Jose E. Roman, Karl Rupp, Patrick Sanan, Jason Sarich, Barry F. Smith, Stefano Zampini, Hong Zhang, PETSc Web Page, (2023). https://petsc.org/.
[29] R.C. Martineau, The MOOSE Multiphysics Computational Framework for Nuclear Power Applications: A Special Issue of Nuclear Technology, Nucl. Technol. 207 (2021) iii–viii. https://doi.org/10.1080/00295450.2021.1915487.
[30] HOME | MOOSE, (n.d.). https://mooseframework.inl.gov/ (accessed December 15, 2021).